ACS Sustainable Chemistry & Engineering

pubs.acs.org/journal/ascecg

Open Access

This article is licensed under CC-BY 4.0

Research Article

Electrodeposited Porous Nickel−Copper as a Non-Noble Metal Catalyst for Urea-Assisted Anion Exchange Membrane Electrolysis for Hydrogen Production

Karuppasamy Dharmaraj,* Rania Hanna, Iver Lauermann, Rory Bagacki, Fanxing Xi, Erno Kemppainen, Rutger Schlatmann, and Sonya Calnan

Cite This: ACS Sustainable Chem. Eng. 2024, 12, 9908−9921

Read Online

ACCESS | Metrics & More | Article Recommendations | Supporting Information

ABSTRACT: Replacing the oxygen evolution reaction with other less energy-intense oxidizing reactions is an attractive option to reduce the energy demand for hydrogen production in an anion exchange membrane (AEM) water electrolyzer using transition metals and their alloys. Since urea is commonly available as a waste product, pairing the urea oxidation at the anode with hydrogen evolution at the cathode in alkaline electrolysis can alleviate environmental issues while simultaneously producing hydrogen. In this respect, we prepared nickel−copper films on nickel felt substrate as a urea oxidation catalyst, which exhibited a lower Tafel slope compared to oxygen evolution, indicating a more favorable reaction pathway. Confirming the improvement, in an AEM electrolyzer, a current density of 50 mA cm^{-2} required a cell voltage of 1.60 V for urea coupled hydrogen production compared to 1.83 V for water oxidation. Nitrogen and carbon dioxide were identified using mass spectrometry (MS) as the main gaseous products during urea electrolysis. A relatively stable zero-gap AEM urea electrolyzer operation at room temperature for over 120 h and at 323.15 K under intermittent power conditions, using nickel−copper catalyst as anode and nickel−molybdenum catalyst as cathode, was demonstrated. Finally, an efficient hydrogen production in the zero-gap alkaline urea electrolyzer at a lower voltage than for water electrolysis was proven using online MS analysis. These results validate the feasibility of reducing the specific energy consumption of electrolyzers used for low-carbon hydrogen production with renewable energy sources.

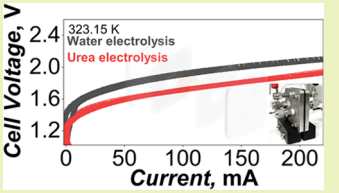

KEYWORDS: *alkaline urea electrolysis, hydrogen evolution reaction, electrocatalysts, membrane electrode assembly, zero-gap electrolyzer*

Downloaded via HELMHOLTZ ZENTRUM BERLIN on December 17, 2024 at 12:56:13 (UTC).
See https://pubs.acs.org/sharingguidelines for options on how to legitimately share published articles.

INTRODUCTION

Alkaline water electrolysis is one of the sustainable ways to produce hydrogen using catalysts composed of abundantly available materials such as nickel, iron, and copper, as well as their alloys. Alkaline water electrolysis proceeds according to the following reactions

$$\text{oxygen evolution reaction (OER): } 4OH^- \rightarrow O_2 + 2H_2O + 4e^-, \quad E^\theta = +0.40 \text{ V vs SHE} \tag{1}$$

$$\text{hydrogen evolution reaction (HER): } 4H_2O + 4e^- \rightarrow 2H_2 + 4OH^-, \quad E^\theta = -0.83 \text{ V vs SHE} \tag{2}$$

$$\text{overall reaction: } 2H_2O \rightarrow 2H_2 + O_2, \quad E^\theta = -1.23 \text{ V} \tag{3}$$

However, the slow reaction kinetics of the oxygen evolution reaction (OER) at the anode elevate the overall voltage needed for the net electrochemical water splitting reaction, leading to a higher energy consumption for sustainable hydrogen production. This limitation can be overcome by replacing the energy-intensive OER with easily oxidizable molecules such as alcohols, urea, ammonia, amines, etc., to produce hydrogen at a lower energy consumption.[1,2] Furthermore, utilizing hydrogen-carrying chemicals (2−2.5 wt %) from waste environments not only alleviates environmental pollution but also yields hydrogen.[3,4] Urea has gained attention due to its substantial hydrogen content (6.67 wt %), cost-effectiveness, and lower theoretical thermodynamic voltage for urea oxidation compared to conventional water electrolysis (1.23 V).[5,6] Urea electrolysis produces N_2, which is nontoxic, and CO_2 which can be used as a high-purity feedstock for chemical or fuel synthesis. In alkaline media, under standard conditions, the thermodynamic potential of urea oxidation reaction (UOR) at the anode is −0.746 V vs SHE while that of the hydrogen evolution reaction (HER) at the cathode is −0.83 V vs SHE. The corresponding half equations are given below:

$$\text{UOR on the anode: } CO(NH_2)_2 + 6OH^- \rightarrow N_2 + 5H_2O + CO_2 + 6e^- \tag{4}$$

Received: March 22, 2024
Revised: June 4, 2024
Accepted: June 5, 2024
Published: June 14, 2024

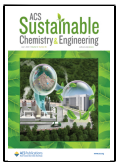

© 2024 The Authors. Published by American Chemical Society

HER on cathode: $6H_2O + 6e^- \rightarrow 3H_2 + 6OH^-$ (5)

overall reaction: $CO(NH_2)_2 + H_2O \rightarrow N_2 + CO_2 + 3H_2$ (6)

The UOR can be efficiently catalyzed by noble metals, but, as large-scale use demands cost-effectiveness, transition metals (TMs) are an attractive alternative option.[4,7−9] Nickel-based electrocatalysts have been reported for UOR, but improvements such as use of a conventional method to prepare catalysts on a large scale and using low-cost precursor materials, without compromising the activity and durability of the electrocatalysts, are needed. Nickel is an example of a nonprecious metal that is an effective electrocatalyst for UOR and whose catalytic activity can be tuned by the synthesis method and by tailoring the surface properties to improve further catalytic efficiency.[10−12] Nickel-based alloys like nickel−cobalt (NiCo),[13,14] nickel−molybdenum (NiMo),[15−18] nickel−copper (NiCu),[19−21] nickel−iron (NiFe),[22,23] and TM sulfides, phosphides, fluorides, nitrides, and analogues[24−29] have been also reported to increase the reaction kinetics of UOR. Specifically, alloying with a second element has proven to be an effective approach to tune d-band electronic properties[21,30] and has been extensively studied for water electrolysis catalysts that could provide an understanding to further develop better urea electrolysis catalysts. For example, copper attracts e_g orbital electrons on iron which further weakens the intermediate species adsorption.[31] Furthermore, in situ Raman studies on Ni confirmed that, in the first step, Ni^{2+} ($Ni(OH)_2$) electrochemically oxidizes to Ni^{3+} (NiOOH), which acts as an active site to dissociate the urea molecule followed by chemical reduction of Ni^{3+} back to Ni^{2+}[32] Due to the high oxidation potential, the inactive Ni^{2+} electrochemically oxidizes back (regeneration) into active Ni^{3+} (NiOOH) which can further dissociate the urea molecules.[32] In particular, α-$Ni(OH)_2$ has a superior catalytic activity to β-$Ni(OH)_2$ for urea electrolysis since the γ-NiOOH/α-$Ni(OH)_2$ redox couple enables efficient electron transfer.[33] These observations imply that the active center for UOR is Ni^{3+} (NiOOH) characterized by its high-valence state, rather than the Ni^{2+} valency state. Therefore, alloying the nickel with a second transition metal is a simple and effective approach to increase the catalyst efficiency for UOR.

Role of Cu and Mo in UOR and HER. In addition to catalytic activity, the potential catalysts must be durable to withstand real-world operating conditions, that is, be insensitive to catalyst poisoning and efficiently drive UOR electrolysis under constant or intermittent power supply (e.g., photovoltaic or wind energy coupled electrolysis).[34−36] During the urea electrolysis, the intermediate products (CO and other carbonaceous intermediates) may adsorb on and deactivate the catalyst active sites before forming the CO_2. In addition, CO desorption from the catalyst is one of the rate-determining steps in the six-electron transfer process in UOR.[37] In this aspect, Cu possesses excellent resistance against persistent adsorption of CO intermediates by effectively promoting the CO desorption which is primarily needed to develop the highly stable urea electrolysis catalysts.[38,39] Cu also decreases the energy requirements for urea adsorption, promoting the oxidation of the energetically favorable *$NHCONH_2$ intermediate by altering the electronic structure of the surrounding Ni sites.[40] Cu disturbs the OH^- ions density which effectively allows the adsorption of urea, facilitating the N−N coupling to form N_2 as the major product. This improves the selectivity to N_2 and not the NO_x compounds.[40,41] Another recent study showed that CuO modulates the electronic states of Ni, which results in Ni−O bonds stretching thus promoting urea molecule dissociation.[42] On the other hand, the performance of a urea electrolyzer is also affected by the cathode reaction, that is alkaline HER for which several TMs and their alloy-based catalysts were already reported with high-current operation.[43,44] Among the TMs, NiMo alloy has proven to be a highly durable industrial use catalyst for alkaline HER allowing stable continuous and intermittent operation.[34,45,46] The activity of NiMo catalysts originates from the interfaces of alloy oxides and hydroxides that can weaken the HO−H bond of absorbed water to facilitate water dissociation in the heterointerfaces by minimizing the free energy for hydrogen adsorption.[47] Mo has been proven to have effective corrosion resistance in alkaline medium via passivation, and the adsorption of MoO can promote the HER activity on Ni.[48−50] Therefore, both Cu and Mo provide an electronic synergy and increased activity toward catalysis when alloyed with Ni.

Based on the above considerations, we prepared NiCu as a UOR catalyst and NiMo as an HER catalyst on nickel fiber felt (NF) via electrodeposition. Then, the prepared NiCu catalyst was electrochemically activated to enhance the active hydroxyl and oxyhydroxyl species on the surface and studied for the urea electrolysis reaction. Following this, both NiCu and NiMo were applied as the anode and cathode catalysts, respectively, in an alkaline anion exchange membrane urea electrolyzer. The electrolyzer was additionally operated under voltage cycling to demonstrate performance stability over 120 h. Simultaneously, the gaseous byproducts generated at different voltages during the electrolyzer operation were also analyzed using mass spectrometry. The structural and compositional changes of the catalysts were also characterized on pre- and postelectrolysis to understand the causes of degradation after extended operation.

RESULTS AND DISCUSSION

Morphological and Structural Characterization of the Catalysts. Nickel is easily converted into $Ni(OH)_2$ in alkaline medium (containing KOH or NaOH), and at alkaline anodic reactions, the valence state of nickel is usually equivalent to that of nickel oxides and oxyhydroxides.[51] Over the course of an electrochemical reaction, the catalyst may suffer irreversible (morphology) and reversible (phase transformation) changes so that the prepared pristine catalyst characteristics are altered after the tests.[52] In this context, the electrodeposited NiCu was electrochemically oxidized in 1.0 M KOH alkaline medium prior to the UOR studies (Figure S1). After 100 cycles of cyclic voltammetry (CV), the deposited catalyst attains a stable voltammogram. The electrochemical activation step causes surface restructuring presumably via dissolution-redeposition and thereby enhances the NiCu hydroxyl and oxyhydroxyl species on the surface.[53,54] This was further confirmed with X-ray photoelectron spectroscopy (XPS) analysis, which will be discussed later. To explore the effect of adding Cu to Ni, the precursor ratios of nickel and copper in the solutions used for electrodeposition were varied (Figure S2) and electrochemical UOR catalytic analysis of the resultant material was carried out. The solution used for electrodeposition consisted of 0.3 M $C_6H_5Na_3O_7{\cdot}2H_2O$, 1.0 M $(NH_4)_2SO_4$, and different molar ratios of $NiSO_4{\cdot}6H_2O$ and $CuSO_4{\cdot}5H_2O$: 0.175/0.08, 0.075/0.025, 0.025/0.075.[55] Herein, the corresponding samples were named as $Ni_{0.175}Cu_{0.08}$, $Ni_{0.075}Cu_{0.025}$, and $Ni_{0.025}Cu_{0.075}$,

https://doi.org/10.1021/acssuschemeng.4c02424
ACS Sustainable Chem. Eng. 2024, 12, 9908−9921

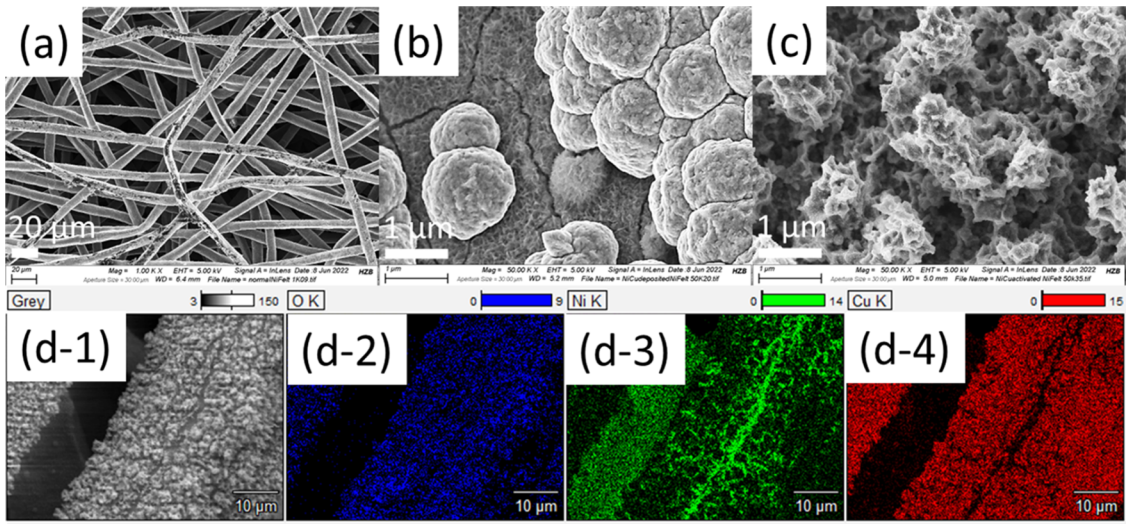

Figure 1. SEM images of (a) cleaned NF, (b) electrodeposited $Ni_{0.175}Cu_{0.08}$ on NF, (c) electrochemically activated $Ni_{0.175}Cu_{0.08}$, and (d-1−d-4) EDX elemental mapping corresponding to SEM of electrochemically activated $Ni_{0.175}Cu_{0.08}$.

respectively. The catalysts deposited using precursors with three different Ni/Cu compositions exhibited a similar performance for alkaline UOR. However, the best performance was observed for $Ni_{0.175}Cu_{0.08}$ compared to the other NiCu and plain Ni catalysts. About 135 mg of $Ni_{0.175}Cu_{0.08}$ was loaded on NF (1.0 cm^2) as determined by subtracting the weight of the dried bare NF before from that coated by electrodeposition.

Scanning electron microscopy (SEM) images show that the NF has a fibrous structure (Figure 1a) while the electrodeposited $Ni_{0.175}Cu_{0.08}$ has a three-dimensional (3-D) nodular structure (Figure 1b).[56] The surface of electrodeposited $Ni_{0.175}Cu_{0.08}$ took on a porous dendritic structure after electrochemical activation in 1.0 M KOH as shown in Figure 1c. Energy-dispersive X-ray (EDX) elemental mappings confirmed a uniform distribution of oxygen, Cu, and Ni. (Figure 1d-1−d-4). The elemental weight percentage of activated $Ni_{0.175}Cu_{0.08}$ is 25 and 63 atom % of Ni and Cu, respectively (Figure S3). Wavelength-dispersive X-ray fluorescence spectroscopy (XRF) was used to confirm the elemental atomic composition of Ni/Cu (atom %:atom %) of $Ni_{0.175}Cu_{0.08}$, $Ni_{0.075}Cu_{0.025}$, and $Ni_{0.025}Cu_{0.075}$ as 38:62, 53:47, and 18:82, respectively. The phase structures of three different Ni to Cu catalysts and their corresponding electrochemically activated samples were characterized using GI-XRD. As shown in Figure 2, the $Ni_{0.175}Cu_{0.08}$ and electrochemically activated $Ni_{0.175}Cu_{0.08}$ contain several crystalline phases. The peaks at 44.48, 51.82, and 76.34° are consistent

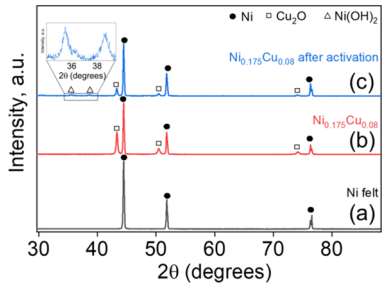

Figure 2. GI-XRD patterns of (a) cleaned NF, (b) electrodeposited $Ni_{0.175}Cu_{0.08}$, and (c) electrochemically activated $Ni_{0.175}Cu_{0.08}$.

with 111, 200, and 220 reflections of nickel's fcc phase (ICDD 00−04−0850) and the peaks at 43.3, 50.46, and 74.16° are representative of fcc copper (ICDD 01−070−3039).[57] The appearance of small peaks after the electrochemical activation at 38.62 and 35.5° correspond to the (101) reflection of β-$Ni(OH)_2$, and the (111) reflection of α-$Ni(OH)_2$, respectively.[58] The new hydroxide peaks further confirmed that the prepared $Ni_{0.175}Cu_{0.08}$ catalysts had undergone a structural change, possibly on the surface, during the electrochemical cycling from Ni^{2+} to Ni^{3+} and back to Ni^{2+} and attained a NiCu-$(OH)_2$ phase. Similar crystalline phases were found for the $Ni_{0.075}Cu_{0.025}$, and $Ni_{0.025}Cu_{0.075}$ catalysts (Figure S4). The electrochemically activated Ni (a-Ni-NF) confirmed the presence of the β-$Ni(OH)_2$ phase (Figure S4). The most active catalyst (for urea electrolysis), $Ni_{0.175}Cu_{0.08}$, was used for further studies and will henceforth be represented as NiCu-NF and its corresponding electrochemically activated as a-NiCu-NF, unless otherwise specified.

XPS measurements were performed on the surface of the NiCu-NF catalyst to understand the chemical composition changes before and after electrochemical activation. Figure S5 shows the XPS spectrum of a wide region of NF, NiCu-NF, and a-NiCu-NF. In Figure 3a, the peaks located at 857.10 and 874.85 eV in the Ni 2p spectrum of NiCu-NF are assigned to Ni^{3+} and the peaks at 855.79 and 873.65 eV are designated to Ni^{2+} species.[20,59,60] While this allocation is quite common in the literature, it is also highly debatable due to the multiple splitting of the photoemission peaks of both Ni^{2+} and Ni^{3+}, which leads to a large number of additional peaks and a very complicated envelope structure, which is not easy to deconvolute.[61] For the sake of simplicity, we therefore use the assignment described above while we are aware of the problems that this can cause in quantification. The Cu $2p_{3/2}$ spectrum of NiCu-NF was deconvoluted into several peaks at 932.68, 952.13 eV and 934.77, 954.72 eV which match the Cu^+ and Cu^{2+} states, respectively (Figure 3b).[20,62−64] After the electrochemical oxidation, there is a distinct intensity increase of the Ni and Cu species which confirms a surface enrichment of $Ni(OH)_2$, CuO, and $Cu(OH)_2$ species after the electrochemical cycling in KOH. It is well reported that the NiO films quickly form $Ni(OH)_2$ on exposure to alkaline medium and

https://doi.org/10.1021/acssuschemeng.4c02424
ACS Sustainable Chem. Eng. 2024, 12, 9908−9921

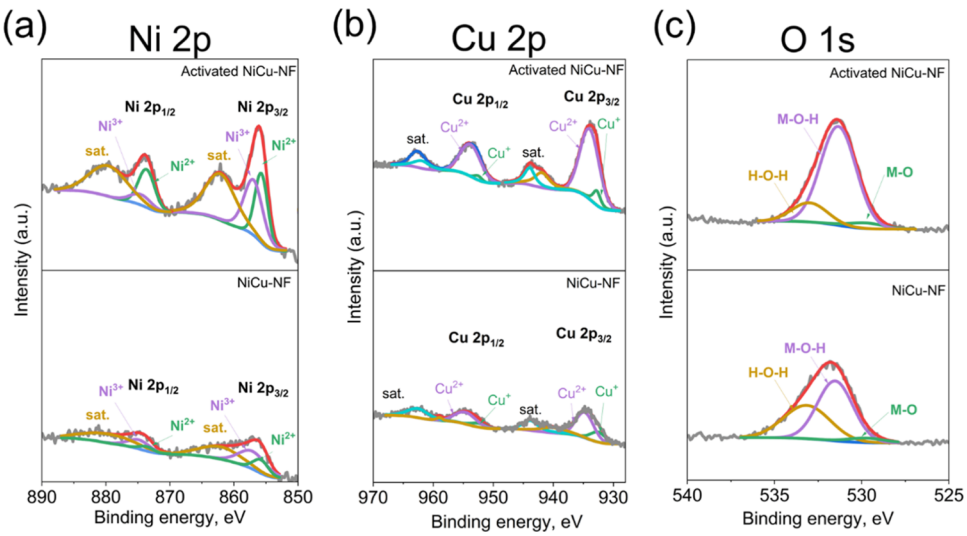

Figure 3. Primary core-level XPS spectra for (a) Ni 2p, (b) Cu 2p, and (c) O 1s, of the a-NiCu-NF (top row) and NiCu-NF (bottom row).

applying a bias voltage of approximately 1.4 V vs RHE results in the formation of NiOOH.[65] Furthermore, the peaks of Ni and Cu species shifted by a few eV before and after the electrochemical activation. For example, the peak at 874.85 eV of NiCu-NF shifted by 0.34 eV to 874.51 eV after the electrochemical activation, suggesting a reduction in the electronegativity of the atoms bonded to Ni. In contrast, the Cu^{2+} peak at 934.77 eV shifted to 934.02 eV after the electrochemical activation, indicating an increase in the electronegativity of the atoms bonded to Cu. This was possibly due to the interaction of Cu and Ni species on the surface[54,60] and may be interpreted as a concurrent reduction and increase in the number of oxygen neighbors of Ni and Cu, respectively. This is also seen with the increase in the size of the Ni^{2+} peak relative to that of Ni^{3+} accompanied by an increase in the size of the peak corresponding to Cu^{2+} relative to that of Cu^{+} after electrochemical activation. The peaks at 529.76, 531.52, and 533.15 eV were ascribed to M−O (M−Ni or Cu), M−OH (M−Ni or Cu), and adsorbed H_2O molecules, respectively.[53,66] In Figure 3c, the ratio of the M−OH peak area relative to that of the M−O peak in the O 1s spectrum of a-NiCu-NF was higher than that of the starting NiCu-NF confirming the formation of NiCu-$(OH)_2$-NF after electrochemical oxidation. The enhancement of M−OH species was consistent with the presence of a-Ni-NF (Figure S6). Also, the deconvoluted area of the Ni^{2+} and Ni^{3+} species after the electrochemical activation of a-NiCu-NF further confirmed the rearrangement of the surface of the prepared electrocatalyst and the enhanced concentration of hydroxyl species on the surface (Table S1).

The electrodeposited NiMo on Ni fiber felt (NiMo-NF) exhibits a fine platelike structure, and after the electrochemical cycling for 20 cycles between −0.5 and −2.0 V vs Hg/HgO (1.0 M KOH), the surface transformed into a uniform 3-D rough structure (Figure 4a,b). The elemental weight percentage determined by XRF of NiMo is 79 and 30 atom % of Ni and Mo, respectively. The XPS survey spectra of NiMo catalysts are presented in Figure S7. Figure 4c,4d presents the high-resolution XPS spectra of electrodeposited NiMo and the electrochemically activated NiMo catalyst (a-NiMo-NF). The peaks observed at 855.59 and 873.37 eV can be attributed to the Ni^{2+} states, whereas the peaks at 856.48 and 874.74 eV

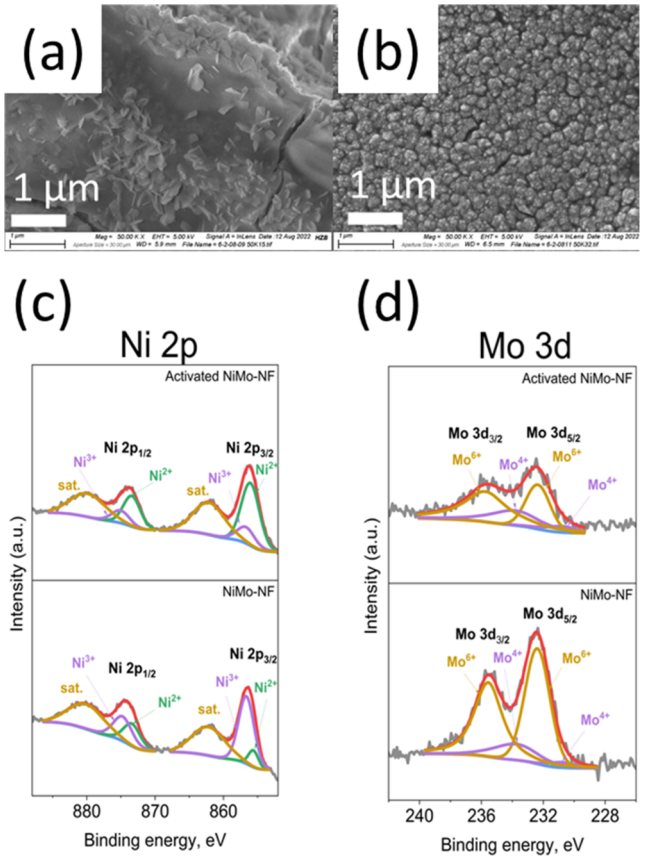

Figure 4. SEM images of (a) electrodeposited NiMo-NF, (b) electrochemically activated NiMo-NF, and (c, d) primary core-level XPS spectra for Ni 2p and Mo 3d of NiMo-NF and a-NiMo-NF.

correspond to Ni^{3+} states in the electrodeposited NiMo. These results agree with those observed in other Ni-based catalysts.[59] Following the electrochemical activation, we observed an increase in the Ni^{2+} content, accompanied by a decrease in the Ni^{3+} content. This correlation arises from the electrochemical activation occurring at the cathodic side, that is, reduction reaction. Peaks at 856.68, 875.04 eV and 856.04, 873.40 eV correspond to the Ni^{3+} and Ni^{2+} states of a-NiMo-NF,

https://doi.org/10.1021/acssuschemeng.4c02424
ACS Sustainable Chem. Eng. 2024, 12, 9908−9921

respectively. For the Mo 3d spectra, the peaks at 230.63 and 233.79 eV are ascribed to Mo^{4+} (MoO_2) and the peaks at 232.35 and 235.64 eV are to Mo^{6+} (MoO_3) states.[67−69] The content of Mo^{4+} in relation to Mo^{3+} did not change significantly after activation. Thus, a-NiMo-NF consisted of bimetallic oxide species of Ni and Mo on the surface.

Electrochemical Characterization of the Catalysts. The a-NiCu-NF and a-NiMo-NF electrocatalysts were characterized by the presence and absence of urea in KOH for UOR and HER, respectively. Though nickel is also highly active for urea electrooxidation, the addition of a small amount of copper further increases the activity of the urea electrolysis in alkaline medium (Figure S2). The enhanced activity of UOR after Cu addition on Ni has been reported already in some studies.[19−21,70] For the a-NiCu-NF electrode (Figure 5a), the anodic peak at 1.37 V vs RHE corresponds to a

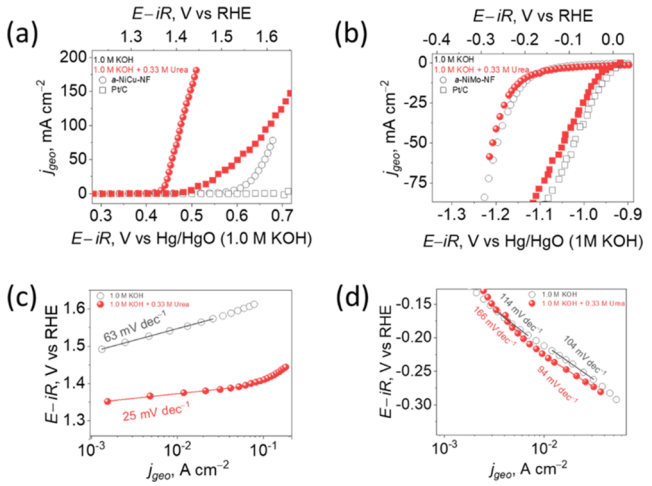

Figure 5. Steady-state polarization curves determined from chronoamperometry response of (a) a-NiCu-NF (○, ●), Pt/C (□,■) for UOR and (b) a-NiMo-NF (○, ●), Pt/C (□,■) for HER in 1.0 M KOH in the presence and absence of 0.33 M urea at 298.15 K. Semilog plots for Tafel slopes at 298.15 K, derived from SS-CA response, of (c) a-NiCu-NF for UOR and OER and (d) a-NiMo-NF catalysts for HER in 1.0 M KOH in the presence and absence of 0.33 M urea.

transformation of $NiCu^{II}$ to $NiCu^{III}$ in 1.0 M KOH which was also observed during the electrochemical activation step (Figure S1).[53] It can be seen in Figure 5a, that in the presence of urea, the geometric current density j_{geo} reached a maximum value of 180 mA cm^{-2} at 1.45 V vs RHE, exhibiting high catalytic activity. The related current density (j_{ECSA}) calculated with respect to the electrochemical surface area (ECSA) is shown in Figure S8. The onset potential of a-NiCu-NF for UOR is 1.35 V vs RHE which is in agreement with the value previously reported Ni alloy catalysts[15,20,22,24] and CuO catalysts (Table S2).[71] In the absence of urea, that is, for the electrooxidation of water, a-NiCu-NF catalyst needs 1.61 V vs RHE to reach 78 mA cm^{-2} compared to 1.40 vs RHE for UOR. The graphs in Figure 5a show that the a-NiCu-NF has a lower onset potential for urea oxidation than Pt/C catalysts.[72]

In the case of HER, the a-NiMo-NF electrode achieved a value of j_{geo} of 30 mA cm^{-2} at −0.26 V vs RHE as shown in Figure 5b. Figure S8 shows the corresponding current density−potential plots derived from ECSA. When urea was added, there was an increase in the overpotential by 12 mV at j_{geo} = 30 mA cm^{-2}. The increase in overpotential in the presence of urea is caused by the adsorption of amino and carbonyl groups from urea onto the Mo reactive sites which could reduce catalytic activity toward HER because Mo is also an effective UOR catalyst.[17] Other researchers also reported a 10 mV increase in overpotential for the HER in the presence of 0.5 M urea for the nickel phosphide catalysts.[73] Compared to Pt/C, a-NiMo-NF showed an overpotential of 170 mV for HER at j_{geo} = 50 mA cm^{-2} (Figure 5b). The addition of Mo to Ni lowers the overpotential by about 200 mV for HER at j_{geo} = 10 mA cm^{-2} (Figure S9).[74] Steady-state chronoamperometry (SS-CA) measurements were performed to determine the Tafel slopes. For the a-NiCu-NF electrode, a Tafel slope of 25 mV dec^{-1} was obtained for the UOR at relatively low current densities (Figure 5c). This agrees with the recently reported article from Zhang, et al. (23 mV dec^{-1}).[21] The lower Tafel slopes revealed faster UOR kinetics, due to the enrichment of $-(OH)_2$ and −OOH active sites on the surface in the KOH medium.[32] Some other UOR catalysts show Tafel slopes in the range between 19 and 50 mV dec^{-1}[18,71] and these differences may arise because of differences in techniques used to acquire the data, corrections for internal resistance, and/or choice of the fitting region. As the potential gets more positive, we observe a loss in linearity of the relationship between $\log j_{geo}$ and *E-iR*, probably due to a change in the rate-determining step caused by either a change in surface coverage of adsorbed species or the commencement of an additional reaction, likely the OER or even the corrosion of Cu. In the absence of urea, a-NiCu-NF catalyst exhibited a Tafel slope of 63 mV dec^{-1} within the oxygen evolution region, consistent with that of documented NiCu catalysts.[66] This lies close to the slope value of 60 mV dec^{-1}, which confirms that the second reaction step is the rate-determining step, that is *OH → *O.[75] Thus, the lower Tafel slope of the UOR indicates more favorable catalytic kinetics than those of the OER. Turning to the HER, in the low-overpotential region, the a-NiMo-NF electrode exhibited a Tafel slope of 114 mV dec^{-1} (Figure 5d). This suggests that the Volmer step ($* + H_2O + e^- \rightarrow H^* + OH^-$) is rate-limiting, agreeing well with observations for other NiMo catalysts.[74,76,77] In the presence of urea, the Tafel slope increased to 166 mV dec^{-1} reflecting a change in the reaction kinetics. Furthermore, at high overpotentials, the Tafel slopes of the a-NiMo-NF catalyst almost converge reaching 94 and 104 mV dec^{-1} for 1.0 M KOH with and without 0.33 M urea added. This observation suggests that the presence of a small urea content does not significantly impact the hydrogen evolution kinetics at higher overpotentials, given that HER relies on water as the reactant. The apparent activation energies for the a-NiCu-NF and a-NiMo-NF samples (Figure S10) were calculated using the Arrhenius equation, $\frac{\partial \log(i_o)}{\partial\left(\frac{1}{T}\right)} = -\frac{E_{app}}{2.3R}$, where i_o is the exchange current density, T is the temperature, E_{app} is the apparent activation energy, and R is the universal gas constant. For a-NiCu-NF in 1.0 M KOH, the E_{app} was determined to be 43 and 41 kJ mol^{-1}, respectively, in the absence and presence of 0.33 M urea. Conversely, for the a-NiMo-NF catalyst, the corresponding E_{app} was found to be 28 and 49 kJ mol^{-1} in the absence and presence of urea, respectively, which are close to previous reports. For example, Shinagawa et al. reported E_{app} of Ni and NiCu alloy of 22 and 57 kJ mol^{-1}, respectively, for HER.[78] Tasic et al. also reported the NiMo catalysts exhibited an E_{app} of 22 kJ mol^{-1} for HER.[79] Notably, Mo facilitates the binding of urea's carbonyl group,

https://doi.org/10.1021/acssuschemeng.4c02424
ACS Sustainable Chem. Eng. 2024, 12, 9908−9921

thereby suppressing the HER activity of the catalyst.[15,17] The E_{app} of the a-NiCu-NF catalyst in the context of both the OER and UOR remains the same. This observation is in concordance with findings in certain Ni-based catalysts for OER.[80] However, when compared to other NiCu-based UOR catalysts, our calculated value is notably higher than the value reported by Zhang et al. (20 kJ mol^{-1}).[21] Since activation energy data for Ni-based UOR catalysts are relatively scarce, direct comparisons are challenging. We also tested the activity of a-NiCu-NF catalysts at different urea concentrations, specifically, 0.05 and 1.0 M, in 1.0 M KOH (Figure S11). The current density increases with the concentration of urea for a given potential vs Hg/HgO. Significantly, the kinetics of urea electrolysis are dependent on the KOH concentration, particularly at higher urea concentrations.[37,81] A density functional theory analysis by Daramola et al. elucidates that the rate-determining steps in urea dissociation are dependent upon hydroxide ions. Moreover, the comparable binding energies of urea molecules and hydroxide ions exert an apparent impact on molecular adsorption onto the catalyst surface.[37]

Single-Cell Test and Gas Analysis. To make comparisons with other reported studies, two-electrode measurements without a membrane were employed, with a-NiCu-NF as the anode and a-NiMo-NF as the cathode, respectively. In our two-electrode measurements, 1.60 V is required for anodic urea electrolysis to achieve 100 mA cm^{-2}, 260 mV less than that required to achieve the same current density by anodic water electrolysis, clearly demonstrating the efficiency of urea electrolysis (Figure S12). The catalytic performance of a-NiCu-NF and a-NiMo-NF was also consistent with those of other nickel-based catalyst studies (Table S3). Yu. et al. reported that Ni−Mo−O catalysts for urea electrolysis required 1.55 V to reach 100 mA cm^{-2}.[18] Zhuo et al. reported that Ni_3S_2−$NiMoO_4$ catalysts effectively catalyzed the UOR, requiring 1.47 V to reach 100 mA cm^{-2}.[28] Lu et al. reported that phosphorized $CoNi_2S_4$ catalysts reached 100 mA cm^{-2} at 1.4 V.[29] It is worth noting that our catalysts were prepared in a facile one-step electrodeposition process, and their performance is comparable to that reported in studies for hydrogen production through urea and other oxidants (Table S4).

To emulate real-world conditions, the durability of the urea electrolysis catalyst performance was further evaluated with a zero-gap single-cell electrolyzer, with the anode and cathode separated by an FAA-3−50 anion exchange membrane (Figure S13) operated at room temperature and at 323.15 K. Aqueous solutions of 1.0 M KOH and 1.0 M KOH containing 0.33 M urea were used as catholyte and anolyte, respectively. At room temperature, as shown in Figure 6a, UOR-coupled HER electrolysis proceeded with a cell voltage that was 200 mV lower than that of conventional alkaline water electrolysis (OER coupled HER). The urea electrolyzer required 1.77 V to reach 100 mA cm^{-2}. We tested for the stability of the cell by varying the applied voltage at periodic intervals (Open circuit voltage (OCV), 1.6 and 1.8 V; each for 10 min) to mimic the fluctuations typical of photovoltaic coupled electrolysis conditions. Variations in the cell performance with time were observable, at the upper cell voltage of 1.8 V (Figure 6c). For the first 3 days, we replaced the spent electrolyte with a fresh one after 24 h, and for the remaining 2 days of testing, the electrolyte was neither changed nor replenished. During the cell operation, at a cell voltage of 1.8 V, the electrolyzer achieved a current density of 75 mA cm^{-2} at the start and this

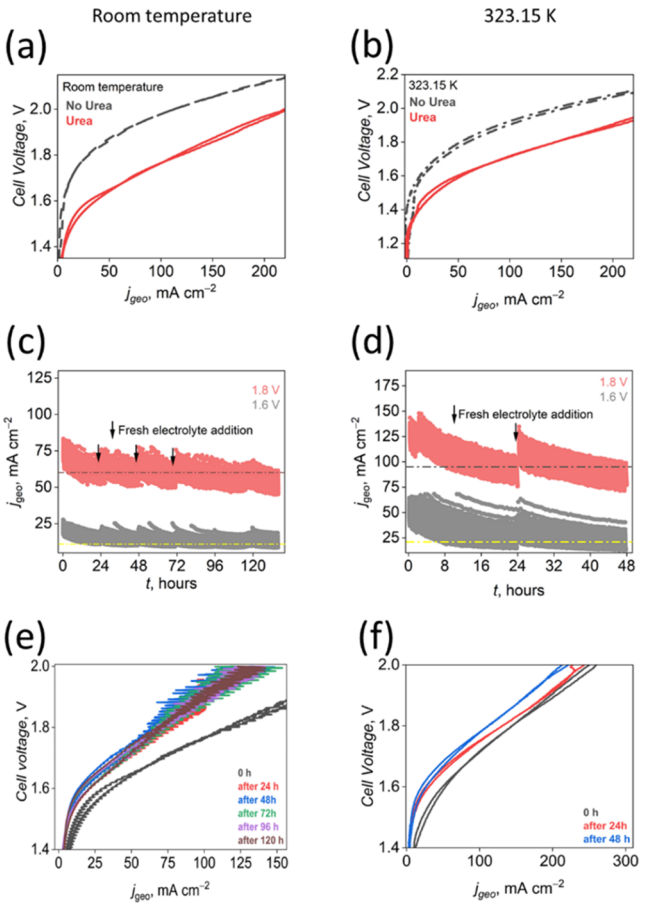

Figure 6. Polarization curves scanned at 10 mV s^{-1} in 1.0 M KOH and in 1.0 M KOH containing 0.33 M urea at (a) room temperature and (b) 323.15 K operation. Intermittent electrolyzer operation between OCV, 1.6 and 1.8 V with a hold of 10 min at (c) room temperature and (d) 323.15 K. Polarization curves at 10 mV s^{-1} measured at the end of specific periods after replenishing the electrolyte in 1.0 M KOH and 0.33 M urea at (e) room temperature and (f) 323.15 K.

gradually decreased to 55 mA cm^{-2} over the space of 24 h. After the feeds were replaced with fresh urea electrolyte, the current density recovered to higher values as confirmed for the first 3 days of operation. The variation in current densities between 0 and 24 h after the electrolyte replenishment is likely due to catalyst restructuring and activation processes during the first day of electrolyzer operation (Figure 6e). After 72 h of electrolyzer operation, the performance gradually decreased mainly due to the consumption of urea in the electrolyte and probably blockage of the active catalyst sites with intermediates. We believe that the former was more likely because the polarization curves measured at specific periods of time after 72 h did not significantly vary from each other (Figure 6e). This was further confirmed with Nyquist plots from electrochemical impedance spectroscopy (EIS) measurements that show no significant changes in the uncompensated resistance, that is, the anion exchange membrane (AEM) did not degrade (Figure S14a−c) at different time intervals during the test. At low current densities tested after 24 and 48 h of cell operation, two arcs were observed, indicating kinetic limitations at both the anode and the cathode. After 96 h operation, the lower-frequency arc diminished, leaving one with an almost unvaried charge transfer resistance. At higher

https://doi.org/10.1021/acssuschemeng.4c02424
ACS Sustainable Chem. Eng. 2024, 12, 9908−9921

current densities, the spectra all had a single-arc feature with a smaller charge transfer resistance than at the lower cell voltage of 1.6 V and no differences were observed over time. This confirms that although the cell performance changed, the urea electrolysis, specifically the catalyst performance, remained stable for over 120 h of intermittent operation at room temperature.

To simulate the challenging conditions of high-temperature environments, the electrolyzer was subjected to testing at 323.15 K. Under these elevated temperature conditions, operating at 1.80 V, j_{geo} is 94 mA cm^{-2}, which is 40 mA cm^{-2} higher than that operating at room temperature (Figure 6b). The increase in temperature certainly improved the reaction kinetics. During the cell operation at 1.80 V, the current density started at 150 mA cm^{-2} and drastically reduced to 75 mA cm^{-2} at the end of day. Then, the anolyte (KOH with urea) was refreshed, allowing the electrolyzer to regain its performance (Figure 6d). In contrast to room-temperature operation, the electrolyzer exhibited a decline in performance over the 24 h, primarily because of the significantly higher consumption of urea (~85%), as evidenced by the polarization curves acquired at various time intervals (as shown in Figure 6f). This was further corroborated by the Nyquist plots, which showed no changes at the OCV (Figure S14d). In Figure S14e, a clear increase in charge transfer resistance arising from the catalyst kinetics toward reaction was observed at the end of the day's operation after the electrolyte was replenished. Additionally, it was noted, especially at high-current-density operation, that the series resistance progressively increased over time, suggesting a possible change in resistance within the membrane, given that the cell remained stable throughout the operation period (Figure S14f). The change in catalyst kinetics was further confirmed with the Nyquist plots after operation for 24 h (Figure S15). Following the electrolyte replenishment, the charge transfer resistance decreased compared to the resistance at the end of day; nevertheless, it did not attain the value at the zeroth hour of testing. Notably, at an electrolyzer voltage of 1.8 V, there were no significant changes observed, likely attributed to the OER as OH^- acts as a reactant.

The gas products of the zero-gap urea electrolyzer operation at room temperature were analyzed by using a JEOL INFITOF mass spectrometer. As depicted in Figure 7, the MS signals exhibit high intensities of N_2 and CO_2 at 1.6 V, indicating the decomposition of urea into CO_2 and N_2 gaseous products under the urea electrolyzer operating conditions. Upon increasing the cell voltage to 1.8 V, an O_2 signal was identified,

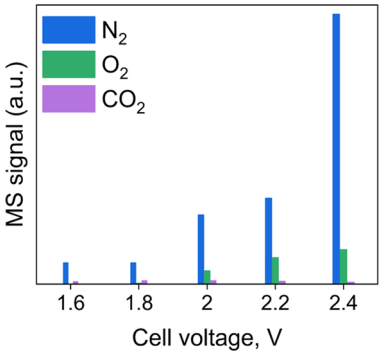

Figure 7. Signal intensity of urea electrolysis products detected by mass spectrometry from the anode at different electrolyzer voltages during room-temperature operation.

suggesting the occurrence of water electrolysis in conjunction with urea electrolysis. Further increases in electrolyzer voltages, specifically at ≥2.0 V, resulted in clear O_2 signals along with N_2 and CO_2 gaseous products. No other byproducts were observed under these operating conditions (Figures S16 and S17). The intensity of CO_2 gas is comparatively lower than the N_2 gas signal, and this may be ascribed to losses arising from the immediate formation of CO_3^{2-} in the OH^- environment, driven by thermodynamically favorable reaction energy (ΔG^o = −56 kJ mol^{-1}), in conjunction with losses via AEM crossover.[82,83] Moreover, step voltages were applied for over 2 h to monitor the intensity of MS signals. Figure 8a,b shows the MS signals for water electrolysis and urea electrolysis, respectively. The hydrogen signal from the cathode in both water and urea electrolysis decreased with a decrease in the applied voltages, indicating a decrease in the volume of produced hydrogen over time. The MS signals for CO_2 and O_2 showed a slight decreasing trend, unlike the N_2 signal, which followed the trend of applied voltages during the urea electrolyzer's operation. Considering an electrolyzer fed with the urea-containing electrolyte and an operating voltage of 1.8 V, N_2, CO_2, and O_2 were detected as gaseous products. In water electrolyzer mode, at lower voltages, the MS signals for H_2 and O_2 approached zero, indicating minimal gas production. At higher voltages, the expected H_2 and O_2 MS signals were measured. Actual quantification of the gaseous products is difficult because, under normal operating conditions, the 1.0 cm^2 electrolyzer size produces relatively low amounts of gas. Additionally, some of the produced gas might dissolve in the electrolyte, causing electrolyte saturation with the remaining gas being available for detection.[84] Nevertheless, under these conditions, we did not detect any gas crossover MS signals, that is, H_2 on the anode exhaust nor N_2, CO_2, and/or, O_2 on the cathode side.

Postmortem Analysis of Catalysts—Structural and Material Characterization. The catalysts utilized in the electrolyzer operation were tested to analyze their condition following the voltage variation test, employing structural and material characterization techniques. Figure 9 shows the SEM images of the anode and cathode catalyst surfaces, which reveal structural changes after intermittent operation. In particular, the highly porous structure of the a-NiCu-NF transitioned into a flat plate configuration both at room temperature (Figure 9b) and during operation at 323.15 K (Figure 9c). In contrast, the structure of a-NiMo-NF remained relatively unaltered, as evidenced in Figure 9d−f. Furthermore, EDX analysis confirmed substantial alterations in the elemental distribution on the catalysts' surfaces, as summarized in Table 1. In the case of the a-NiCu-NF catalyst, a decrease in Cu content was observed, while K and O were enriched. Additionally, a trace amount of Fe (0.32 atom %) was detected following the urea electrolyzer operation, likely stemming from the KOH electrolyte (either already containing some iron or that dissolved from the electrolyzer end plates) used during room-temperature operation over a period of 5 days.[85,86] These findings align with results obtained from surface-sensitive XPS analysis, as illustrated in Figure 10a,10c. Conversely, for the cathode a-NiMo-NF catalyst, we observed a noticeable reduction in the concentration of the Mo content within the catalyst structure. However, the alterations in the composition of other elements did not follow a consistent pattern across both operating temperatures. This variance could be attributed to several factors, including the inherent

https://doi.org/10.1021/acssuschemeng.4c02424
ACS Sustainable Chem. Eng. 2024, 12, 9908−9921

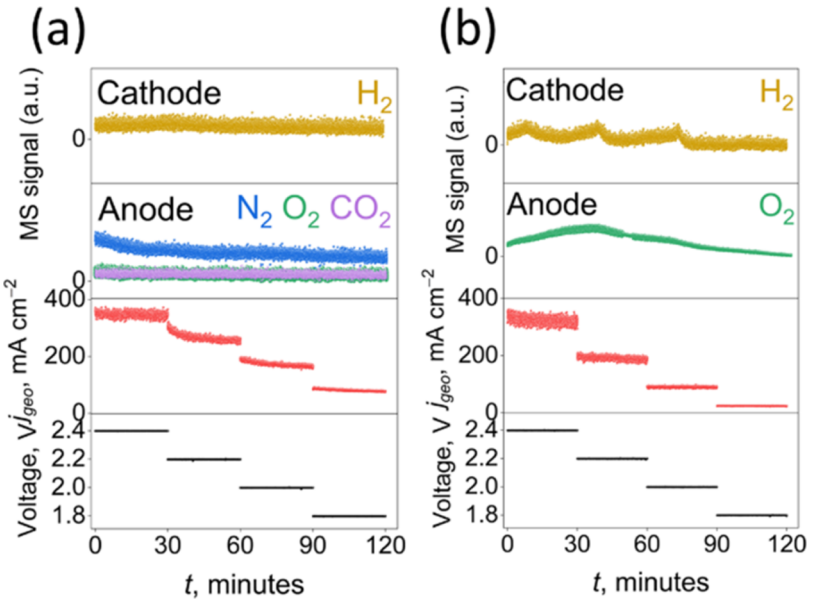

Figure 8. Time evolution of the gaseous products of (a) urea and (b) water electrolyzer operation in response to varying and holding the cell voltage for steps of 30 min.

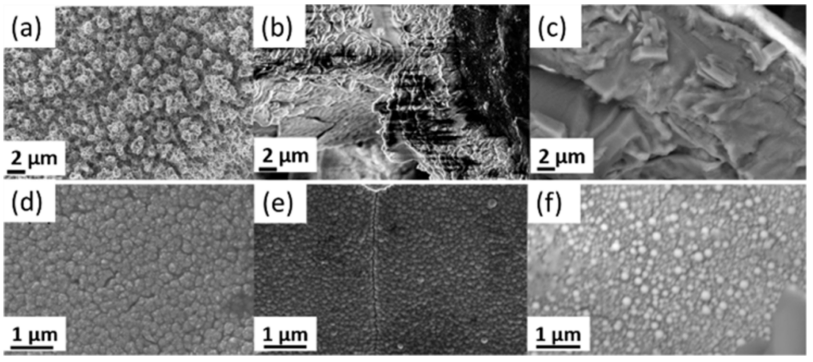

Figure 9. SEM images of a-NiCu-NF (a–c) and a-NiMo-NF (d–f), catalysts fresh (a, d), 5 days of intermittent operation in a urea electrolyzer at room temperature (b, e), and 2 days of intermittent operation in a urea electrolyzer at 323.15 K (c, f).

Table 1. Elemental Composition Determined from EDX Analysis before and after Intermittent Operation in an Alkaline Urea Electrolyzer

catalysts	a-NiCu-NF				a-NiMo-NF			
elemental atomic %	Ni	Cu	O	K	Ni	Mo	O	K
0 h, prior to operation	24.84	62.91	11.23	1.03	63.21	4.70	28.97	3.13
operation at room temperature	29.13	4.36	61.52	4.68 (Fe-0.32)	82.26	3.37	13.70	0.67
operation at 323.15 K	17.76	2.02	61.43	18.79	56.91	0.42	35.95	6.72

sensitivity of the EDX technique, which may lead to variations in the measured elemental content. Additionally, the challenges associated with precisely replicating measurement locations before and after the testing regime can introduce some degree of uncertainty. Interestingly, our XPS measurements provided further insights and clearly revealed a reduction in the presence of molybdenum oxides on the catalyst's surface as shown in Figure 10b. These observations signify the dynamic nature of transformations within the catalysts, exerting an influence on both their elemental composition and structural attributes as they depend on the conditions of the operational environment. Overall, the NiCu catalyst showed significant stability under intermittent operation over at least 48 h at elevated temperature (323.15 K) in alkaline AEM urea-assisted hydrogen production via electrolysis. The incorporation of Cu, its resistance to CO poisoning, and the presence of $Ni(OH)_2$ at oxidation potentials enhance the oxidation of urea effectively.

Other researchers achieved 100 mA cm^{-2} at 1.50 V on slightly larger 4 cm^2 electrodes with a Sustainion X37–50 anion exchange membrane at room temperature.[24] The UOR catalyst used in that case was nickel ferrocyanide whose deposition took at least 24 h. In comparison, we used a-NiCu-NF and a-NiMo-NF catalysts, grown in a few minutes by electrodeposition, albeit on smaller 1.0 cm^2 electrodes, and reached 100 mA cm^{-2} at 1.8 and 1.7 V at room temperature and 323.15 K, respectively, with an FAA-3–50 membrane. Though our electrolyzer was smaller and perhaps not as

https://doi.org/10.1021/acssuschemeng.4c02424
ACS Sustainable Chem. Eng. 2024, 12, 9908–9921

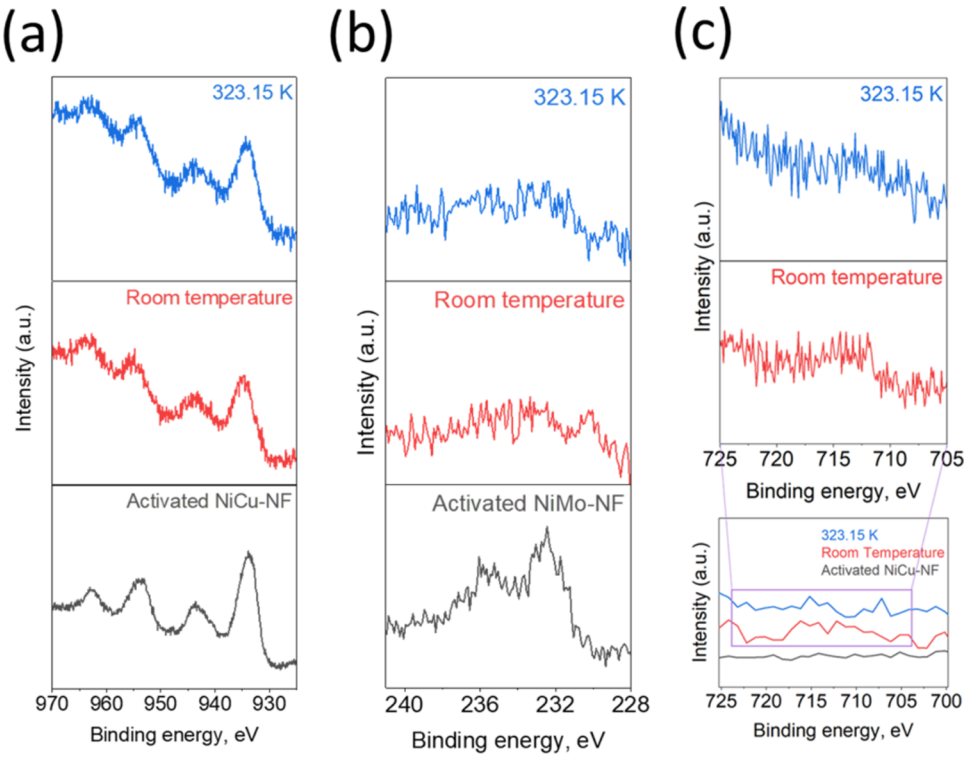

Figure 10. High-resolution XPS spectra of Cu 2p core level of (a) a-NiCu-NF, (b) Mo 3d core level of a-NiMo-NF, and (c) Fe 2p core-level impurities of a-NiCu-NF measured after the single UOR/HER cell tests at room temperature and 323.15 K. The corresponding spectra of the activated catalysts in a state just before the commencement of the test are included as a reference.

efficient, we went a step further to demonstrate relatively stable operation under cyclic conditions at room and elevated temperatures, unlike the previous report. In contrast to several other reports, our research involved the identification of gaseous products directly from the zero-gap alkaline urea electrolyzer through online MS. Also, the dynamic voltage cycling test of the catalysts at room and 323.15 K operation in a zero-gap cell clearly represents a step forward toward practical real-world applications. The post characterization analysis elucidates the dynamic nature of the electrocatalysts under realistic operating conditions. Finally, the tested urea electrolyzer cell showed sustained H_2 production at a lower voltage than the alkaline water electrolyzer, which was further confirmed with MS measurements.

CONCLUSIONS

In summary, we successfully prepared NiCu and NiMo bimetallic catalysts via electrodeposition and subsequent activation in an alkaline medium to enhance the active $-(OH)_2$ species on the catalyst surface. Due to the simplicity of electrodeposition, these catalysts can be prepared beyond the lab scale (e.g., 100 cm^2 area) to test in electrolyzers at semi-pilot scale. The prepared electrocatalysts, a-NiCu-NF and a-NiMo-NF employed as anode and cathode in an alkaline urea electrolyzer cell, need only 1.65 V to reach 50 mA cm^{-2} at room temperature. In addition, under intermittent operating conditions at both room temperature and 323.15 K, the electrodes showed relatively high stability toward urea electrolysis. This study demonstrates that NiCu and NiMo bimetallic catalysts are promising catalytic materials for low-energy hydrogen production from alkaline urea-assisted water splitting. Gas analysis measurements confirmed nitrogen and carbon dioxide as byproducts of urea electrolysis and the sustained hydrogen generation, even at cell voltages that are usually too low for that in water electrolysis. Postmortem material characterization analysis confirmed that the catalyst activity was relatively stable under intermittent operating conditions despite ex situ observation of the structural and elemental composition changes after several hours of operation. These catalytic materials may potentially allow more efficient photovoltaic coupled urea electrolysis because of the significant reduction in the voltage to drive electrolysis with UOR instead of an OER at the anode to produce hydrogen at a relatively lower electrolyzer input power. This work also paves the way for the development of alternative electrocatalysts for efficient urea electrolysis characterized by enhanced stability and activity.

EXPERIMENTAL SECTION

Chemicals and Materials. For this study, the following chemicals were used without any further purification (Table 2).

Nickel fiber felt (Bekipor Nickel, 20 μm fiber diameter, 0.5 mm thickness, 80% porosity from NV Bekaert SA Bekaert Fiber Technologies) and Fumasep FAA-3−50 (45−55 μm thickness, from FUMATECH BWT GmbH) anion exchange membranes (AEM) were used as catalyst supports and the ion conducting half-cell separator, respectively, in an electrolysis cell. All electrolytes were prepared using deionized water (DI) with a resistivity of 18.2 MΩ·cm obtained from a Barnstead Smart2Pure Pro Water Purification System (Thermo Scientific).

Electrodeposition. Prior to the electrodeposition, the NF was cleaned by ultrasonicating it for 10 min each in the following sequence of solvents: first in 25% HCl, followed by DI water, acetone, DI water, isopropanol, and finally again with DI water.

Electrodeposition of NiCu on NF and Electrochemical Activation. The electrochemical bath used to grow NiCu contained 0.08 M $CuSO_4{\cdot}5H_2O$, 0.175 M $NiSO_4{\cdot}6H_2O$, 0.3 M $C_6H_5Na_3O_7{\cdot}2H_2O$ and 1.0 M $(NH_4)_2SO_4$. The pH of the electrolyte was adjusted

https://doi.org/10.1021/acssuschemeng.4c02424
ACS Sustainable Chem. Eng. 2024, 12, 9908−9921

Table 2. Chemicals and Their Intended Uses in This Study

no.	chemical name and details	purpose
1	acetone (≥99% Technical, VWR Chemicals)	cleaning
2	ammonia (20% (wt %, as NH_3) for analysis, PanReac AppliChem)	pH adjustment
3	ammonium sulfate ($(NH_4)_2SO_4$, Baker analyzed ACS reagent, J.T.Baker)	electrodeposition
4	copper(II) sulfate pentahydrate ($CuSO_4·5H_2O$, ≥98.5%, purified, VWR Chemicals)	electrodeposition
5	deionized water (18.2 MΩ·cm, Thermo Scientific)	cleaning, electrolyte
6	hydrochloric acid ((HCl), 25% for analysis EMSURE, Merck)	cleaning, pH adjustment
7	isopropanol (≥98% Technical, VWR Chemicals)	cleaning
8	nickel(II) sulfate hexahydrate ($NiSO_4·6H_2O$, ≥98%, extra pure, Carl Roth GmbH + Co. KG)	electrodeposition
9	potassium chloride 3.0 M (KCl, Metrohm Deutschland)	reference electrode filling solution
10	potassium hydroxide (KOH, pellets EMPLURA, Merck)	electrolyte
11	sodium citrate tribasic dihydrate ($C_6H_5Na_3O_7·2H_2O$, puriss. p.a., ACS reagent, ≥99.0%, Sigma-Aldrich)	electrodeposition
12	sodium molybdate dihydrate ($Na_2MoO_4·2H_2O$, ≥99%, pure, Carl Roth GmbH + Co. KG)	electrodeposition
13	platinum, 10% on carbon, dry (Alfa Aesar)	catalyst
14	fumion (FAA-3) solution (Fuel cell store)	catalyst preparation
15	urea (GR for analysis ACS, Reag. Ph Eur)	electrolyte

to 4.0 with a FiveEasy F20 pH meter (Mettler-Toledo AG). The galvanostatic electrodeposition was performed under stirring at 300 rpm by using the NF (1.0 cm × 1.0 cm as deposition area), an Ag/AgCl electrode (double junction, Metrohm) filled with 3.0 M KCl and nickel foam (>99.99% purity, 1.6 mm thickness, ≥95% porosity, Nanografi, 3.0 cm × 5.0 cm) as the working, reference, and counter electrodes, respectively. A constant current density of −20 mA cm^{-2} was applied for 1800 s by using a Parstat 4000+ potentiostat (AMETEK, Inc.). The electrodeposited catalyst was activated to restructure the catalyst surface via electrochemical cycling using the CV technique. The procedure consisted of 3 CV cycles at 20 mV s^{-1}, followed by 200 CV cycles at 100 mV s^{-1}, and then 3 CV cycles at 20 mV s^{-1} between the potentials 0 to 0.8 V vs a reference electrode consisting of Hg/HgO filled with 1.0 M KOH (Pine Research Instrumentation) (Figure S1).

Electrodeposition of NiMo on NF and Electrochemical Activation. The electrodeposition of NiMo was carried out using the same equipment as that for NiCu. The electrolyte bath used to grow the NiMo catalyst contained 0.030 M $NiSO_4·6H_2O$, 0.020 M $Na_2MoO_4·2H_2O$, and 0.030 M $C_6H_5Na_3O_7·2H_2O$.[74] The galvanostatic electrodeposition was performed under stirring at 300 rpm by using the NF (1.0 cm × 1.0 cm as deposition area); an Ag/AgCl electrode filled with 3.0 M KCl and nickel foam (3.0 cm × 5.0 cm area) were used as working, reference, and counter electrodes, respectively. A constant current density of −24 mA cm^{-2}, respective to the geometric area of the working electrode, was applied for 1800 s. The electrodeposited catalysts were activated for 20 cycles between −0.5 and −2.0 V vs Hg/HgO (1.0 M KOH) at 100 mV s^{-1}.

Pt/C Preparation on NF. 1.0 mg portion of Pt/C was dispersed in 500 μL of 2-propanol, 500 μL of distilled water, and 100 μL of 5% Fumion (FAA-3) solution and ultrasonicated for 60 min to acquire the homogeneous suspension. Afterward, the ink was spread onto a piece of NF (1.0 cm^2) and dried.

Structural Characterization. Scanning electron microscopy (SEM) images and energy-dispersive X-ray (EDX) measurements of the catalyst-coated NF were collected using a Leo Gemini 1530 instrument from Zeiss. The elemental composition was measured by wavelength-dispersive X-ray fluorescence (XRF) by using a Rigaku Primus II+ system. The crystalline structure of the prepared electrocatalysts was analyzed by grazing incidence X-ray diffraction (GI-XRD) using a Bruker AXS D8 Advance X-ray diffractometer with Cu Kα radiation (λ = 0.15406 nm). The incidence angle for GIXRD was set to 1°, the step size to 0.02°, and the time per step to 1 s. X-ray photoelectron spectroscopy (XPS) was performed on the prepared catalysts to determine their surface chemical composition in the CISSY setup at the BESSY II synchrotron in Berlin.[87] Mg Kα radiation of 1253.6 eV was used as the excitation source. The detailed results of the XPS measurements are presented in the Supporting Information (Table S5).

Electrocatalytic Studies. For the three-electrode measurements, a Hg/HgO electrode filled with 1.0 M KOH (Pine Research Instrumentation) and graphite plate (4.0 cm × 4.0 cm, Alfa Aesar) were used as reference and counter electrodes, respectively. The three-electrode electrochemical measurements were carried out by using a Zennium E4 potentiostat (Zahner, Germany). To test the single-cell electrolyzer, a Biologic SP-150 (Biologic, France) or Parstat 4000+ (AMETEK) was used. The onset potentials were determined by measuring 5 times the baseline current. For the temperature variation measurements, a Hg/HgO reference electrode filled with 1.0 M KOH from ALS Co., Ltd. was used, in which the electrode was kept at room temperature and connected with the ceramic tip liquid junction filled with 1.0 M KOH, to keep the reference electrode potential constant irrespective of the electrolyte temperature. The Hg/HgO reference electrode was calibrated with respect to the reversible hydrogen electrode (RHE) as follows. The Hg/HgO (1.0 M KOH) and the RHE (HydroFlex from Gaskatel GmbH, Germany) used as reference and working electrodes, respectively, and a platinum wire as the counter electrode, were immersed in N_2-saturated 1.0 M KOH for at least 2500 s. Then, the offset potential was determined by recording the constant open circuit potential ((OCP) calibration value), which was found to be 0.934 V (Figure S18). This was used to correct the Hg/HgO electrode against RHE in 1.0 M KOH as follows: $E_{RHE} = E_{Hg/HgO} + 0.934$ V. Chronoamperometry (CA) for 120 s was used to acquire each data point for the polarization curves. The integral area of the redox peak method was used for the electrochemical surface area (ECSA) calculations.[88]

Determination of Tafel Slopes. A series of SS-CA were carried out to acquire the Tafel slope plots.[89] The CA technique was used to apply constant potentials for 120 s, ranging from 0.30 to 0.80 V vs Hg/HgO (1.0 M KOH), with an increment of 20 mV. In our case, the mean of the last 20 s was chosen for each potential for the Tafel plot. For the cathodic reaction, i.e., HER studies, negative potentials were applied and calculated in the same manner. Then, the measured currents were corrected to remove the uncompensated resistance (100% *iRs* corrected). The uncompensated resistance was determined using EIS which was measured between the frequency range from 100 kHz to 10 mHz with an amplitude of 10 mV at 0.40 V. For the SS-CA, in our case, the electrolyte was stirred under 300 rpm using a magnetic bead to prevent mass transport limitations.

Two-Electrode Measurements. Two-electrode measurements were conducted to test the stability performance of the catalyst at the preliminary stage. An a-NiCu-NF (active area: 1.0 cm × 1.0 cm) and a-NiMo-NF (active area: 1.0 cm × 1.0 cm) electrode were connected via a tantalum contact sample holder (Redoxme AB) as an anode and a cathode, respectively. The 1.0 cm wide spacing between the anode and cathode was filled with 1.0 M KOH with or without the addition of 0.33 M urea. The electrolyte was mixed using mild stirring (300 rpm), and its temperature of the electrolyte was determined to be 298.15 K. Intermittent operation was mimicked by applying 1.25 V for 10 min followed by applying 1.65 V for another 10 min across the electrodes, and this cycle was repeated for 48 h. The electrolyte was replaced with fresh 1.0 M KOH containing 0.33 M urea after 24 h to compensate depletion of the urea during operation.

Single-Cell Test. The durability of the a-NiCu-NF electrode was tested using an in-house developed 1.0 cm^2 electrode area zero-gap full electrolyzer cell. For this, a-NiCu-NF as anode and a-NiMo-NF as cathode separated by an FAA-3−50 AEM were used for urea electrolysis. Ethylene propylene diene monomer (EPDM) gaskets were used to seal the cell, and a bolt torque of 1.5 N-m was applied to

https://doi.org/10.1021/acssuschemeng.4c02424
ACS Sustainable Chem. Eng. 2024, 12, 9908−9921

the screws of the cell to ensure leak tightness and a low ohmic contact resistance between the flow fields and the electrodes. The FAA-3−50 AEM was activated by soaking it in 0.5 M KOH for at least 24 h before the single-cell measurements. Peristaltic pumps (Watson-Marlow GmbH) were used to feed the cell with 1.0 M KOH containing 0.33 M urea as anolyte and 1.0 M KOH as catholyte, both, at a flow rate of 15 mL min^{-1}. The cell was subjected to cyclic operation by first measuring the OCV for 10 min, followed by applying a constant voltage of 1.6 V for another 10 min, then applying 1.8 V for another 10 min, and this cycle was repeated for several loops. EIS measurements were performed from 100 kHz to 20 mHz with a 10 mV amplitude at open circuit and at selected applied voltages.

Gas Analysis. Gas analysis was performed by continuous sampling of the cell output via 100 μm inner diameter capillary tubing (Agilent Technologies) connected to the sample insertion interface of a mass spectrometer MS (INFITOF JMS-MT3010HRGA, JEOL, Japan). The spectrometer is configured with a two-turn flight path, 50 μA ion current, 100 °C ion chamber temperature, and 70 V ionization voltage. ALPHAGAZ 1 ARGON (Ar ≥ 99.999) from Air Liquide was used as the carrier gas. A schematic illustration of the gas analysis setup is shown in Figure S19. Before initiating the measurements, the KOH electrolytes were purged with argon for at least 90 min, both in the presence and absence of urea. Subsequently, the electrolyte was circulated within the cell, which was accompanied by a continuous purge of argon. This process was continued until the elimination of excess gases, ensuring the exclusive detection of the argon signal in the MS. For the detection of UOR products, constant voltages were applied for 30 min, and then the MS signals were measured.

■ ASSOCIATED CONTENT

Supporting Information

The Supporting Information is available free of charge at https://pubs.acs.org/doi/10.1021/acssuschemeng.4c02424.

Additional XRD; XPS and electrochemical characterization; XPS experimental details; photographs of experimental setup; and MS spectra (PDF)

■ AUTHOR INFORMATION

Corresponding Author

Karuppasamy Dharmaraj − *Institute Competence Centre Photovoltaics Berlin, Helmholtz-Zentrum Berlin für Materialien und Energie GmbH, 12489 Berlin, Germany;* orcid.org/0000-0001-6743-3503;
Email: karuppasamy.dharmaraj@helmholtz-berlin.de

Authors

Rania Hanna − *Institute Competence Centre Photovoltaics Berlin, Helmholtz-Zentrum Berlin für Materialien und Energie GmbH, 12489 Berlin, Germany*

Iver Lauermann − *Institute Competence Centre Photovoltaics Berlin, Helmholtz-Zentrum Berlin für Materialien und Energie GmbH, 12489 Berlin, Germany;* orcid.org/0000-0002-9119-3770

Rory Bagacki − *Institute Competence Centre Photovoltaics Berlin, Helmholtz-Zentrum Berlin für Materialien und Energie GmbH, 12489 Berlin, Germany*

Fanxing Xi − *Institute Competence Centre Photovoltaics Berlin, Helmholtz-Zentrum Berlin für Materialien und Energie GmbH, 12489 Berlin, Germany*

Erno Kemppainen − *Institute Competence Centre Photovoltaics Berlin, Helmholtz-Zentrum Berlin für Materialien und Energie GmbH, 12489 Berlin, Germany;* orcid.org/0000-0003-3858-020X

Rutger Schlatmann − *Institute Competence Centre Photovoltaics Berlin, Helmholtz-Zentrum Berlin für Materialien und Energie GmbH, 12489 Berlin, Germany;* orcid.org/0000-0002-5951-9435

Sonya Calnan − *Institute Competence Centre Photovoltaics Berlin, Helmholtz-Zentrum Berlin für Materialien und Energie GmbH, 12489 Berlin, Germany*

Complete contact information is available at: https://pubs.acs.org/10.1021/acssuschemeng.4c02424

Author Contributions

S.C. proposed the idea, supervised the project, reviewed the manuscript, and acquired financial support. K.D. and S.C. conceived the idea and experimental direction. K.D. planned the experiments, analyzed the original data, and collected measurement data from other authors. K.D. also wrote the original draft. R.H. performed all three-electrode electrochemical experiments. I.L. conducted XPS experiments, and K.D. analyzed the spectra and engaged in discussions with I.L. R.H. and R.B. conducted the single-cell test room-temperature measurements. R.H. and K.D. conducted the single-cell test 323.15 K measurements. F.X. and R.H. were responsible for collecting SEM images. F.X. and K.D. performed XRD measurements. E.K. provided suggestions for experimental direction, aided in the visualization of data, and reviewed the manuscript. R.S. acquired financial support and reviewed the manuscript. All authors provided critical feedback and given their approval for the final version of the manuscript

Notes

The authors declare no competing financial interest.

■ ACKNOWLEDGMENTS

The authors acknowledge the support from the German Federal Ministry of Education and Research (BMBF) in the framework of the project CatLab (03EW0015A). They also thank Christian Schary, Iris Dorbandt, and Maximilian Reinhardt for logistical assistance in organizing the electrochemical experiments.

■ REFERENCES

(1) Pethaiah, S. S.; Sadasivuni, K. K.; Jayakumar, A.; Ponnamma, D.; Tiwary, C. S.; Sasikumar, G. Methanol Electrolysis for Hydrogen Production Using Polymer Electrolyte Membrane: A Mini-Review. *Energies* **2020**, *13* (22), No. 5879.

(2) Wang, L.; Zhu, Y.; Wen, Y.; Li, S.; Cui, C.; Ni, F.; Liu, Y.; Lin, H.; Li, Y.; Peng, H.; Zhang, B. Regulating the Local Charge Distribution of Ni Active Sites for the Urea Oxidation Reaction. *Angew. Chem.* **2021**, *133* (19), 10671−10676.

(3) Lan, R.; Tao, S.; Irvine, J. T. S. A direct urea fuel cell − power from fertiliser and waste. *Energy Environ. Sci.* **2010**, *3* (4), 438−441.

(4) Simka, W.; Piotrowski, J.; Robak, A.; Nawrat, G. Electrochemical treatment of aqueous solutions containing urea. *J. Appl. Electrochem.* **2009**, *39* (7), 1137−1143.

(5) Rollinson, A. N.; Jones, J.; Dupont, V.; Twigg, M. V. Urea as a hydrogen carrier: a perspective on its potential for safe, sustainable and long-term energy supply. *Energy Environ. Sci.* **2011**, *4* (4), 1216−1224.

(6) Boggs, B. K.; King, R. L.; Botte, G. G. Urea electrolysis: direct hydrogen production from urine. *Chem. Commun.* **2009**, No. 32, 4859−4861.

(7) Climent, V.; Rodes, A.; Orts, J. M.; Aldaz, A.; Feliu, J. M. Urea adsorption on Pt (111) electrodes. *J. Electroanal. Chem.* **1999**, *461* (1−2), 65−75.

(8) Shen, H.; Wei, T.; Liu, Q.; Zhang, S.; Luo, J.; Liu, X. Heterogeneous Ni-MoN nanosheet-assembled microspheres for urea-assisted hydrogen production. *J. Colloid Interface Sci.* **2023**, *634*, 730−736.
(9) Wei, T.; Meng, G.; Zhou, Y.; Wang, Z.; Liu, Q.; Luo, J.; Liu, X. Amorphous Fe−Co oxide as an active and durable bifunctional catalyst for the urea-assisted H_2 evolution reaction in seawater. *Chem. Commun.* **2023**, *59* (66), 9992−9995.
(10) Xia, L.; Liao, Y.; Qing, Y.; Xu, H.; Gao, Z.; Li, W.; Wu, Y. *In Situ* Growth of Porous Ultrathin $Ni(OH)_2$ Nanostructures on Nickel Foam: An Efficient and Durable Catalysts for Urea Electrolysis. *ACS Appl. Energy Mater.* **2020**, *3* (3), 2996−3004.
(11) Liu, J.-L.; Zhou, X.-Y.; An, J.-L.; Wang, Y.-Q.; Zhang, M.-D.; Qin, L. One Bifunctional Electrocatalyst Derived from Nickel MOF for Urea Oxidation Reaction and Hydrogen Evolution Reaction. *Energy Fuels* **2022**, *36* (17), 10346−10353.
(12) Yue, Z.; Zhu, W.; Li, Y.; Wei, Z.; Hu, N.; Suo, Y.; Wang, J. Surface Engineering of a Nickel Oxide−Nickel Hybrid Nanoarray as a Versatile Catalyst for Both Superior Water and Urea Oxidation. *Inorg. Chem.* **2018**, *57* (8), 4693−4698.
(13) Huang, W.; Wang, K.; Cao, Q.; Zhao, Y.; Sun, X.; Ding, R.; Liu, E.; Gao, P.; Li, G. Hierarchical NiCo pearl strings as efficient electrocatalysts for urea electrooxidation. *New J. Chem.* **2021**, *45* (6), 2943−2947.
(14) Nguyen, N. S.; Das, G.; Yoon, H. H. Nickel/cobalt oxide-decorated 3D graphene nanocomposite electrode for enhanced electrochemical detection of urea. *Biosens. Bioelectron.* **2016**, *77*, 372−377.
(15) Huang, X.; He, R.; Wang, S.; Yang, Y.; Feng, L. High-Valent Ni Species Induced by Inactive MoO_2 for Efficient Urea Oxidation Reaction. *Inorg. Chem.* **2022**, *61* (45), 18318−18324.
(16) Wang, T.; Miao, L.; Zheng, S.; Qin, H.; Cao, X.; Yang, L.; Jiao, L. Interfacial Engineering of Ni_3N/Mo_2N Heterojunctions for Urea-Assisted Hydrogen Evolution Reaction. *ACS Catal.* **2023**, *13* (7), 4091−4100.
(17) Sha, L.; Liu, T.; Ye, K.; Zhu, K.; Yan, J.; Yin, J.; Wang, G.; Cao, D. A heterogeneous interface on $NiS@Ni_3S_2/NiMoO_4$ heterostructures for efficient urea electrolysis. *J. Mater. Chem. A* **2020**, *8* (35), 18055−18063.
(18) Yu, Z.-Y.; Lang, C.-C.; Gao, M.-R.; Chen, Y.; Fu, Q.-Q.; Duan, Y.; Yu, S.-H. Ni−Mo−O nanorod-derived composite catalysts for efficient alkaline water-to-hydrogen conversion *via* urea electrolysis. *Energy Environ. Sci.* **2018**, *11* (7), 1890−1897.
(19) Yang, S.-B.; Tsai, Y.-C.; Wu, M.-S. Honeycomb-like copper/cuprous oxide with supported nickel hydroxide layer as an electrode material for electrochemical oxidation of urea. *J. Alloys Compd.* **2020**, *836*, No. 155533.
(20) Xie, J.; Gao, L.; Cao, S.; Liu, W.; Lei, F.; Hao, P.; Xia, X.; Tang, B. Copper-incorporated hierarchical wire-on-sheet α-$Ni(OH)_2$ nanoarrays as robust trifunctional catalysts for synergistic hydrogen generation and urea oxidation. *J. Mater. Chem. A* **2019**, *7* (22), 13577−13584.
(21) Zhang, K.; Wang, S.; Li, X.; Li, H.; Ni, Y. Phase Segregation in $Cu_{0.5}Ni_{0.5}$ Alloy Boosting Urea-Assisted Hydrogen Production in Alkaline Media. *Small* **2023**, *19*, No. 2300959.
(22) Yan, L.; Sun, Y.; Hu, E.; Ning, J.; Zhong, Y.; Zhang, Z.; Hu, Y. Facile in-situ growth of Ni2P/Fe2P nanohybrids on Ni foam for highly efficient urea electrolysis. *J. Colloid Interface Sci.* **2019**, *541*, 279−286.
(23) Zhang, J.-J.; Bao, W.-W.; Li, M.-Y.; Yang, C.-M.; Zhang, N.-N. Ultrafast formation of an FeOOH electrocatalyst on Ni for efficient alkaline water and urea oxidation. *Chem. Commun.* **2020**, *56* (93), 14713−14716.
(24) Geng, S.-K.; Zheng, Y.; Li, S.-Q.; Su, H.; Zhao, X.; Hu, J.; Shu, H.-B.; Jaroniec, M.; Chen, P.; Liu, Q.-H.; Qiao, S. Z. Nickel ferrocyanide as a high-performance urea oxidation electrocatalyst. *Nat. Energy* **2021**, *6* (9), 904−912.
(25) Xu, X.; Dong, Y.; Wang, X.; Liu, F.; Ren, J.; Wang, H.; Wang, R. High-Density NiCu Bimetallic Phosphide Nanosheet Clusters Constructed by Cu-Induced Effect Boost Total Urea Hydrolysis for Hydrogen Production. *Inorg. Chem.* **2023**, *62* (11), 4648−4661.
(26) Patil, S. J.; Chodankar, N. R.; Hwang, S. K.; Raju, G. S. R.; Huh, Y. S.; Han, Y. K. Fluorine Engineered Self-Supported Ultrathin 2D Nickel Hydroxide Nanosheets as Highly Robust and Stable Bifunctional Electrocatalysts for Oxygen Evolution and Urea Oxidation Reactions. *Small* **2022**, *18* (7), No. 2103326.
(27) Hu, S.; Wang, S.; Feng, C.; Wu, H.; Zhang, J.; Mei, H. Novel MOF-Derived Nickel Nitride as High-Performance Bifunctional Electrocatalysts for Hydrogen Evolution and Urea Oxidation. *ACS Sustainable Chem. Eng.* **2020**, *8* (19), 7414−7422.
(28) Zhuo, X.; Jiang, W.; Yu, T.; Qian, G.; Chen, J.; Yang, H.; Yin, S. Crystalline−Amorphous Ni_3S_2−$NiMoO_4$ Heterostructure for Durable Urea Electrolysis-Assisted Hydrogen Production at High Current Density. *ACS Appl. Mater. Interfaces* **2022**, *14* (41), 46481−46490.
(29) Lu, X. F.; Zhang, S. L.; Sim, W. L.; Gao, S.; Lou, X. W. D. Phosphorized $CoNi_2S_4$ Yolk-Shell Spheres for Highly Efficient Hydrogen Production via Water and Urea Electrolysis. *Angew. Chem.* **2021**, *133* (42), 23067−23073.
(30) Wang, H.; Liu, X.; Liu, G.; Wang, Y.; Du, X.; Li, J. Copper doping-induced high-valence nickel-iron-based electrocatalyst toward enhanced and durable oxygen evolution reaction. *Chem. Catal.* **2023**, *3*, No. 100552.
(31) Cao, D.; Xu, H.; Cheng, D. Branch-leaf-shaped CuNi@NiFeCu nanodendrites as highly efficient electrocatalysts for overall water splitting. *Appl. Catal., A* **2021**, *298*, No. 120600.
(32) Vedharathinam, V.; Botte, G. G. Direct evidence of the mechanism for the electro-oxidation of urea on Ni (OH) 2 catalyst in alkaline medium. *Electrochim. Acta* **2013**, *108*, 660−665.
(33) Wu, T.-H.; Hou, B.-W. Superior catalytic activity of α-$Ni(OH)_2$ for urea electrolysis. *Catal. Sci. Technol.* **2021**, *11* (12), 4294−4300.
(34) Kemppainen, E.; Aschbrenner, S.; Bao, F.; Luxa, A.; Schary, C.; Bors, R.; Janke, S.; Dorbandt, I.; Stannowski, B.; Schlatmann, R.; Calnan, S. Effect of the ambient conditions on the operation of a large-area integrated photovoltaic-electrolyser. *Sustainable Energy Fuels* **2020**, *4* (9), 4831−4847.
(35) Bao, F.; Kemppainen, E.; Dorbandt, I.; Xi, F.; Bors, R.; Maticiuc, N.; Wenisch, R.; Bagacki, R.; Schary, C.; Michalczik, U.; et al. Host, Suppressor, and Promoter—The Roles of Ni and Fe on Oxygen Evolution Reaction Activity and Stability of NiFe Alloy Thin Films in Alkaline Media. *ACS Catal.* **2021**, *11* (16), 10537−10552.
(36) Calnan, S.; Bagacki, R.; Bao, F.; Dorbandt, I.; Kemppainen, E.; Schary, C.; Schlatmann, R.; Leonardi, M.; Lombardo, S. A.; Milazzo, R. G.; et al. Development of Various Photovoltaic-Driven Water Electrolysis Technologies for Green Solar Hydrogen Generation. *Sol. RRL* **2022**, *6* (5), No. 2100479.
(37) Daramola, D. A.; Singh, D.; Botte, G. G. Dissociation Rates of Urea in the Presence of NiOOH Catalyst: A DFT Analysis. *J. Phys. Chem. A* **2010**, *114* (43), 11513−11521.
(38) Sun, J.; Shi, J.; Xu, J.; Chen, X.; Zhang, Z.; Peng, Z. Enhanced methanol electro-oxidation and oxygen reduction reaction performance of ultrafine nanoporous platinum−copper alloy: Experiment and density functional theory calculation. *J. Power Sources* **2015**, *279*, 334−344.
(39) Hefnawy, M. A.; Fadlallah, S. A.; El-Sherif, R. M.; Medany, S. S. Synergistic effect of Cu-doped NiO for enhancing urea electro-oxidation: comparative electrochemical and DFT studies. *J. Alloys Compd.* **2022**, *896*, No. 162857.
(40) Tatarchuk, S. W.; Medvedev, J. J.; Li, F.; Tobolovskaya, Y.; Klinkova, A. Nickel-Catalyzed Urea Electrolysis: From Nitrite and Cyanate as Major Products to Nitrogen Evolution. *Angew. Chem., Int. Ed.* **2022**, *61* (39), No. e202209839.
(41) Shen, Z.; Qi, Y.; Ge, W.; Jiang, H.; Li, C. Highly Selective Electrooxidation of Urea to Nitrogen on Copper/Nickel Boride Interface under Alkaline Condition. *Ind. Eng. Chem. Res.* **2023**, *62* (22), 8736−8743.
(42) Yang, L.; He, R.; Wang, X.; Yang, T.; Zhang, T.; Zuo, Y.; Lu, X.; Liang, Z.; Li, J.; Arbiol, J.; et al. Self-supported NiO/CuO

https://doi.org/10.1021/acssuschemeng.4c02424
ACS Sustainable Chem. Eng. 2024, 12, 9908−9921

electrodes to boost urea oxidation in direct urea fuel cells. *Nano Energy* **2023**, *115*, No. 108714.
(43) Chen, Z.; Duan, X.; Wei, W.; Wang, S.; Ni, B.-J. Recent advances in transition metal-based electrocatalysts for alkaline hydrogen evolution. *J. Mater. Chem. A* **2019**, *7* (25), 14971−15005.
(44) Li, S.; Li, E.; An, X.; Hao, X.; Jiang, Z.; Guan, G. Transition metal-based catalysts for electrochemical water splitting at high current density: current status and perspectives. *Nanoscale* **2021**, *13* (30), 12788−12817.
(45) Kabir, S.; Lemire, K.; Artyushkova, K.; Roy, A.; Odgaard, M.; Schlueter, D.; Oshchepkov, A.; Bonnefont, A.; Savinova, E.; Sabarirajan, D. C.; et al. Platinum group metal-free NiMo hydrogen oxidation catalysts: high performance and durability in alkaline exchange membrane fuel cells. *J. Mater. Chem. A* **2017**, *5* (46), 24433−24443.
(46) Raja, D. S.; Cheng, C.-C.; Ting, Y.-C.; Lu, S.-Y. NiMo-MOF-Derived Carbon-Armored Ni_4Mo Alloy of an Interwoven Nanosheet Structure as an Outstanding pH-Universal Catalyst for Hydrogen Evolution Reaction at High Current Densities. *ACS Appl. Mater. Interfaces* **2023**, *15* (16), 20130−20140.
(47) Luo, M.; Yang, J.; Li, X.; Eguchi, M.; Yamauchi, Y.; Wang, Z.-L. Insights into alloy/oxide or hydroxide interfaces in Ni−Mo-based electrocatalysts for hydrogen evolution under alkaline conditions. *Chem. Sci.* **2023**, *14* (13), 3400−3414.
(48) Arnaudova, M.; Lefterova, E.; Rashkov, R. Corrosion behavior of electrodeposited nickel-based coatings with W, Mo, and TiOx. *J. Solid State Electrochem.* **2024**, *28* (5), 1657−1670.
(49) Lützenkirchen-Hecht, D.; Frahm, R. Corrosion of Mo in KOH: Time Resolved XAFS Investigations. *J. Phys. Chem. B* **2001**, *105* (41), 9988−9993.
(50) Du, W.; Shi, Y.; Zhou, W.; Yu, Y.; Zhang, B. Unveiling the In Situ Dissolution and Polymerization of Mo in Ni_4Mo Alloy for Promoting the Hydrogen Evolution Reaction. *Angew. Chem., Int. Ed.* **2021**, *60* (13), 7051−7055.
(51) Yeo, B. S.; Bell, A. T. In Situ Raman Study of Nickel Oxide and Gold-Supported Nickel Oxide Catalysts for the Electrochemical Evolution of Oxygen. *J. Phys. Chem. C* **2012**, *116* (15), 8394−8400.
(52) Hales, N.; Schmidt, T. J.; Fabbri, E. Reversible and irreversible transformations of Ni-based electrocatalysts during the oxygen evolution reaction. *Curr. Opin. Electrochem.* **2023**, *38*, No. 101231.
(53) Zhang, H.; Chen, W.; Wang, H.; Tong, X.; Wang, Y.; Yang, X.; Wu, Z.; Liu, Z. A core-shell NiCu@NiCuOOH 3D electrode induced by surface electrochemical reconstruction for the ammonia oxidation reaction. *Int. J. Hydrogen Energy* **2022**, *47* (36), 16080−16091.
(54) Xu, W.; Lan, R.; Du, D.; Humphreys, J.; Walker, M.; Wu, Z.; Wang, H.; Tao, S. Directly growing hierarchical nickel-copper hydroxide nanowires on carbon fibre cloth for efficient electro-oxidation of ammonia. *Appl. Catal., B* **2017**, *218*, 470−479.
(55) Mattarozzi, L.; Cattarin, S.; Comisso, N.; Gambirasi, A.; Guerriero, P.; Musiani, M.; Vazquez-Gomez, L.; Verlato, E. Hydrogen evolution assisted electrodeposition of porous Cu-Ni alloy electrodes and their use for nitrate reduction in alkali. *Electrochim. Acta* **2014**, *140*, 337−344.
(56) Goranova, D.; Avdeev, G.; Rashkov, R. Electrodeposition and characterization of Ni-Cu alloys. *Surf. Coat. Technol.* **2014**, *240*, 204−210.
(57) Eugénio, S.; Silva, T. M.; Carmezim, M. J.; Duarte, R. G.; Montemor, M. F. Electrodeposition and characterization of nickel−copper metallic foams for application as electrodes for super-capacitors. *J. Appl. Electrochem.* **2014**, *44* (4), 455−465.
(58) Hall, D. S.; Lockwood, D. J.; Bock, C.; Macdougall, B. R. Nickel hydroxides and related materials: a review of their structures, synthesis and properties. *Proc. R. Soc. A* **2015**, *471* (2174), No. 20140792.
(59) Mansour, A. N.; Melendres, C. A. Characterization of electrochemically prepared γ-NiOOH by XPS. *Surf. Sci. Spectra* **1994**, *3* (3), 271−278.
(60) Huang, J.; Cai, J.; Wang, J. Nanostructured Wire-in-Plate Electrocatalyst for High-Durability Production of Hydrogen and Nitrogen from Alkaline Ammonia Solution. *ACS Appl. Energy Mater.* **2020**, *3* (5), 4108−4113.
(61) Grosvenor, A. P.; Biesinger, M.; Smart, R.; McIntyre, N. New interpretations of XPS spectra of nickel metal and oxides. *Surf. Sci.* **2006**, *600* (9), 1771−1779.
(62) Deroubaix, G.; Marcus, P. X-ray photoelectron spectroscopy analysis of copper and zinc oxides and sulphides. *Surf. Interface Anal.* **1992**, *18* (1), 39−46.
(63) Parmigiani, F.; Pacchioni, G.; Illas, F.; Bagus, P. S. Studies of the Cu O bond in cupric oxide by X-ray photoelectron spectroscopy and ab initio electronic structure models. *J. Electron Spectrosc. Relat. Phenom.* **1992**, *59* (3), 255−269.
(64) Hernnäs, B.; Karolewski, M.; Tillborg, H.; Nilsson, A.; Mårtensson, N. On the growth of Ni on Cu (100). *Surf. Sci.* **1994**, *302* (1−2), 64−72.
(65) Gallenberger, J.; Fernández, H. M.; Alkemper, A.; Li, M.; Tian, C.; Kaiser, B.; Hofmann, J. P. Stability and decomposition pathways of the NiOOH OER active phase of NiO_x electrocatalysts at open circuit potential traced by *ex situ* and *in situ* spectroscopies. *Catal. Sci. Technol.* **2023**, *13* (16), 4693−4700.
(66) Singh, A.; Schneller, T.; Valov, I.; Singh, I. B.; Srivastava, A. K.; Waser, R. Copper facilitated nickel oxy-hydroxide films as efficient synergistic oxygen evolution electrocatalyst. *J. Catal.* **2020**, *384*, 189−198.
(67) Wang, Y.; Wang, Y.; Bai, J.; Lau, W. M. Efficient Self-Supported Bifunctional NiMo Alloy Electrocatalysts for Water Splitting in Alkaline Environment. *ChemistrySelect* **2022**, *7* (17), No. e202200468.
(68) Moulder, J. F.; Chastain, J. *Handbook of X-ray Photoelectron Spectroscopy: A Reference Book of Standard Spectra for Identification and Interpretation of XPS Data*, Physical Electronics Division; Perkin-Elmer Corporation, 1992; p 221.
(69) Li, C.; Wang, J.; Wang, Y.; Li, J.; Yao, Z.; Jiang, Z. Enhancing Hydrogen Evolution Reaction by Synergistically Coupling NiMo Alloy with $Ni(OH)_2$ Nanosheet on Carbon Cloth. *ChemistrySelect* **2020**, *5* (22), 6774−6779.
(70) Wang, J.; Ma, Y. Copper and nickel-based oxides delicately tailored via galvanic reaction as electrocatalyst for solid-state direct urea fuel cell. *Int. J. Hydrogen Energy* **2023**, *48* (74), 28882−28890.
(71) Wang, Y.; Li, Y.; Ding, L.; Ding, J. A facile oxidation−dehydration reaction-driven robust porous copper oxide nanobelt coating on copper foam for an energy-saving and low-cost urea oxidization reaction. *Chem. Commun.* **2019**, *55* (90), 13562−13565.
(72) Lu, S.; Hummel, M.; Gu, Z.; Wang, Y.; Wang, K.; Pathak, R.; Zhou, Y.; Jia, H.; Qi, X.; Zhao, X.; et al. Highly Efficient Urea Oxidation via Nesting Nano-Nickel Oxide in Eggshell Membrane-Derived Carbon. *ACS Sustainable Chem. Eng.* **2021**, *9* (4), 1703−1713.
(73) Liu, D. N.; Liu, T. T.; Zhang, L. X.; Qu, F. L.; Du, G.; Asiri, A. M.; Sun, X. P. High-performance urea electrolysis towards less energy-intensive electrochemical hydrogen production using a bifunctional catalyst electrode. *J. Mater. Chem. A* **2017**, *5* (7), 3208−3213.
(74) Bao, F.; Kemppainen, E.; Dorbandt, I.; Bors, R.; Xi, F.; Schlatmann, R.; Krol, R.; Calnan, S. Understanding the Hydrogen Evolution Reaction Kinetics of Electrodeposited Nickel-Molybdenum in Acidic, Near-Neutral, and Alkaline Conditions. *ChemElectroChem* **2021**, *8* (1), 195−208.
(75) Fang, Y.-H.; Liu, Z.-P. Tafel Kinetics of Electrocatalytic Reactions: From Experiment to First-Principles. *ACS Catal.* **2014**, *4* (12), 4364−4376.
(76) Cao, J.; Li, H.; Pu, J.; Zeng, S.; Liu, L.; Zhang, L.; Luo, F.; Ma, L.; Zhou, K.; Wei, Q. Hierarchical NiMo alloy microtubes on nickel foam as an efficient electrocatalyst for hydrogen evolution reaction. *Int. J. Hydrogen Energy* **2019**, *44* (45), 24712−24718.
(77) Llorente, V. B.; Diaz, L.; Lacconi, G.; Abuin, G.; Franceschini, E. Effect of duty cycle on NiMo alloys prepared by pulsed electrodeposition for hydrogen evolution reaction. *J. Alloys Compd.* **2022**, *897*, No. 163161.
(78) Shinagawa, T.; Takanabe, K. New Insight into the Hydrogen Evolution Reaction under Buffered Near-Neutral pH Conditions:

https://doi.org/10.1021/acssuschemeng.4c02424
ACS Sustainable Chem. Eng. 2024, 12, 9908−9921

Enthalpy and Entropy of Activation. *J. Phys. Chem. C* **2016**, *120* (42), 24187−24196.
(79) Tasic, G. S.; Maslovara, S. P.; Zugic, D. L.; Maksic, A. D.; Kaninski, M. P. M. Characterization of the Ni-Mo catalyst formed *in situ* during hydrogen generation from alkaline water electrolysis. *Int. J. Hydrogen Energy* **2011**, *36* (18), 11588−11595.
(80) Suffredini, H. B.; Cerne, J. L.; Crnkovic, F. C.; Machado, S. A. S.; Avaca, L. A. Recent developments in electrode materials for water electrolysis. *Int. J. Hydrogen Energy* **2000**, *25* (5), 415−423.
(81) Jia, X.; Kang, H. J.; Yang, X. X.; Li, Y. L.; Cui, K.; Wu, X. H.; Qin, W.; Wu, G. Amorphous Ni(III)-based sulfides as bifunctional water and urea oxidation anode electrocatalysts for hydrogen generation from urea-containing water. *Appl. Catal., B* **2022**, *312*, No. 121389.
(82) Blommaert, M. A.; Subramanian, S.; Yang, K.; Smith, W. A.; Vermaas, D. A. High Indirect Energy Consumption in AEM-Based CO_2 Electrolyzers Demonstrates the Potential of Bipolar Membranes. *ACS Appl. Mater. Interfaces* **2022**, *14* (1), 557−563.
(83) Chang, H.-M.; Zenyuk, I. V. Membrane electrode assembly design to prevent CO_2 crossover in CO_2 reduction reaction electrolysis. *Commun. Chem.* **2023**, *6* (1), No. 2.
(84) Trinke, P.; Haug, P.; Brauns, J.; Bensmann, B.; Hanke-Rauschenbach, R.; Turek, T. Hydrogen crossover in PEM and alkaline water electrolysis: mechanisms, direct comparison and mitigation strategies. *J. Electrochem. Soc.* **2018**, *165* (7), No. F502.
(85) Spanos, I.; Masa, J.; Zeradjanin, A.; Schlögl, R. The Effect of Iron Impurities on Transition Metal Catalysts for the Oxygen Evolution Reaction in Alkaline Environment: Activity Mediators or Active Sites? *Catal. Lett.* **2021**, *151* (7), 1843−1856.
(86) Chung, D. Y.; Lopes, P. P.; Martins, P. F. B. D.; He, H.; Kawaguchi, T.; Zapol, P.; You, H.; Tripkovic, D.; Strmcnik, D.; Zhu, Y.; et al. Dynamic stability of active sites in hydr(oxy)oxides for the oxygen evolution reaction. *Nat. Energy* **2020**, *5* (3), 222−230.
(87) Lauermann, I.; Steigert, A. CISSY: A station for preparation and surface/interface analysis of thin film materials and devices. *J. Large-Scale Res. Facil. JLSRF* **2016**, *2*, No. A67.
(88) Anantharaj, S.; Kundu, S. Do the Evaluation Parameters Reflect Intrinsic Activity of Electrocatalysts in Electrochemical Water Splitting? *ACS Energy Lett.* **2019**, *4* (6), 1260−1264.
(89) Anantharaj, S.; Noda, S.; Driess, M.; Menezes, P. W. The Pitfalls of Using Potentiodynamic Polarization Curves for Tafel Analysis in Electrocatalytic Water Splitting. *ACS Energy Lett.* **2021**, 1607−1611.

https://doi.org/10.1021/acssuschemeng.4c02424
ACS Sustainable Chem. Eng. 2024, 12, 9908−9921